Evaluation of grain boundary energy, structure and stiffness from phase field crystal simulations

Blixt, Kevin; Hallberg, Håkan

[Link to publication](#)

Evaluation of grain boundary energy, structure and stiffness from phase field crystal simulations

Kevin Hult Blixt and Håkan Hallberg*

Division of Solid Mechanics, Lund University, P.O. Box 118, SE-221 00 Lund, Sweden

Abstract

A two-mode phase field crystal (PFC) model is employed to investigate the equilibrium configurations of a range of grain boundaries in FCC-structured materials. A total of 80 different symmetrical tilt grain boundaries are evaluated by PFC simulations in 3D and the results are shown to agree well with data taken from the literature, both regarding the variation of grain boundary energy and also in terms of the resulting grain boundary structures. This verification complements existing PFC studies which are almost exclusively focused either on grain boundaries found in 2D systems or in BCC lattices in 3D. The present work facilitates application of PFC in the analysis of grain boundary mechanics in an extended range of materials, in particular such mechanics that take place at extended time scales not tractable for molecular dynamics simulations. In addition to the verification of predicted grain boundary energies and structures, wavelet transforms of the density field are used in the present work to obtain phase fields from which it is possible to identify grain boundary fluctuations that provide the means to evaluate grain boundary stiffness based on the capillarity fluctuation method. It is discussed how PFC provides benefits compared to alternative methods, such as molecular dynamics simulations, for this type of investigations.

Keywords: Grain boundary, Phase field crystal, Grain boundary energy, Grain boundary structure, Grain boundary stiffness, Capillary fluctuation method

1 Introduction

The properties of crystalline materials are dictated by the state of the material's microstructure, not least by the presence and character of structural defects. Grain boundaries, constituting widespread planar defects in the crystal structure, are of particular importance for a number of microstructure processes including creep and corrosion as well as diffusion and segregation of alloying elements. Grain boundaries are also key factors in defining the material's macroscopic strength and toughness. Grain boundaries are, however, highly heterogeneous microstructure features that carry anisotropic properties which depend on the local microstructure conditions. This anisotropy is clearly manifested by, for example, the grain boundary energy which tend to vary with a set of five degrees of freedom, comprising the local misorientation between abutting

---

*Corresponding author. E-mail: hakan.hallberg@solid.lth.se. Tel.: +46 46 222 90 92.

grains as well as the local inclination of the grain boundary plane [46]. This provides a complex and multi-dimensional energy landscape that defies straightforward handling in numerical models. As a result, this energy variation is usually neglected in mesoscale numerical models of crystal microstructure based on, for example, phase fields, level sets, cellular automata or Monte Carlo Potts and front tracking (vertex) algorithms. Examples of such methods used for microstructure simulations can be found in [26]. If grain boundary energy variations are indeed considered in such models, it is almost exclusively done under limiting simplifications and assumptions. In fact, the grain boundary energy is in most numerical models taken as an isotropic constant, an approach that is certain to render all subsequent calculations questionable, at best. Notable exceptions to such customs are provided by the phase field model discussed in [34], where advantage is taken of the grain boundary energy database established in [35], and by the level set model proposed in [27], where use is made of the GB5DOF algorithm provided in [12]. A proper description of heterogeneous grain boundary properties is of particular importance when considering nanocrystalline materials in which the volume fraction of grain boundaries is high.

The means to provide a more faithful account of local grain boundary property variations are provided by first principle or molecular dynamics (MD) simulations. But when considering microstructure processes such as grain growth or segregation, the associated time scales (hours) are beyond what is feasible to handle using these types of simulation models where the time scale is dictated by the atomic vibration frequency. An alternative numerical tool emerged by the introduction of phase field crystal (PFC) modeling in [17, 18]. The PFC method initially appeared as an elaboration of standard phase field formulations, but it has later been shown that PFC can be derived directly from density functional theory (DFT) [5, 19, 20, 30, 55]. Standard phase field formulations are based on order parameter fields, defined such that they assume different constant values in adjacent and stable phases and vary smoothly across phase interfaces. In contrast, PFC describes a continuous transition of a density field from a homogeneous to a periodic state. This is achieved as the evolution of the density field is governed by a free energy functional that is minimized by a periodic solution, thereby avoiding the spatial averaging over atomic distances inherent in standard phase field formulations. The governing free energy functional can in PFC modeling be designed such that the symmetries of the ground state correlate to a particular crystal structure. As PFC models a time-averaged atomic number density field over diffusive time scales, while retaining atomic-level spatial resolution, the method resides somewhere between standard phase field models and atomistic models.

Many, if not a majority, of the PFC studies published to date have focused on systems involving solid-liquid transitions, including nucleation and growth, melting and glass formation. Different applications of PFC modeling are reviewed in, for example, [7, 20]. PFC-based studies on interfaces between solid phases, such as grain boundaries, are less common. The energy of $\langle 100 \rangle$ tilt boundaries in triangular 2D lattices has been evaluated by PFC in several studies, such as in [17], and a few studies also extend to $\langle 100 \rangle$ tilt boundaries in 3D BCC crystals, for example [3, 31]. It can also be noted that most PFC studies of grain boundaries in BCC materials focus on the low-angle range of grain boundaries. In contrast to what is available for BCC materials, PFC investigations on the energy and structure of grain boundaries in FCC crystals – which is the focus of the present study – are even more scarce. In fact, FCC systems in general are less explored by PFC than BCC systems. This gap is likely much due to that the classical PFC

formalism introduced in [18] will only provide triangular lattices in 2D and BCC structures in 3D. This follows from the "one-mode approximation" upon which the original PFC formalism is built, in which the influence from all but the first density wave length are damped out. For FCC lattices, the classical PFC formulation is insufficient but FCC structures can be achieved by using a "two-mode approximation" as proposed in, for example, [6, 60].

In the present study, the viability of PFC for simulating the structure and energy of grain boundaries in FCC crystals is investigated by considering an extensive set of different grain boundary configurations. In addition, evaluation of grain boundary stiffness is addressed by extracting grain boundary fluctuations from wavelet transforms of the density field. This work complements existing PFC studies on 2D or BCC-structured materials and constitutes a verification step permitting employment of PFC in other types of analyses related to polycrystal microstructures, for example aimed at phenomena such as normal/abnormal grain growth, stress-driven grain boundary migration, grain boundary faceting and grain boundary phase transformations ("complexions"). The evaluation of grain boundary stiffness opens for an even wider range of grain boundary mechanisms for which PFC can be employed.

This paper is structured in such way that the PFC model is discussed first in Section 2 along with details given on the numerical implementation of the model. Next, simulations of a large number of grain boundary configurations in FCC crystals are shown in Section 3. In separate sections, the evaluation of grain boundary energy, structure and stiffness is discussed. Finally, some concluding remarks close the paper in Section 4.

2 Phase field crystal model

The PFC formulation is based on an atomic number density field $\rho(\boldsymbol{r})$, with $\boldsymbol{r}$ denoting the spatial coordinates. This is usually considered as a dimensionless density field $\phi(\boldsymbol{r}) = (\rho(\boldsymbol{r}) - \rho_0)/\rho_0 \equiv \Delta\rho(\boldsymbol{r})/\rho_0$, where ρ_0 is the number density at the homogeneous liquid reference state and where $\Delta\rho(\boldsymbol{r})$ is the density variation around this reference state. By this definition, the order parameter $\phi(\boldsymbol{r})$ represents the time-averaged density of atoms, measured relative to the constant reference value ρ_0. With these preliminaries, a Helmholtz free energy functional can be defined as

$$\mathcal{F}(T, [\phi(\boldsymbol{r})]) = \left(\int_V f\left(\phi(\boldsymbol{r})\right) d\boldsymbol{r} \right)\bigg|_T \tag{1}$$

where $f\left(\phi(\boldsymbol{r})\right)$ is the free energy density evaluated at temperature T in a system of volume V.

For a system with interacting particles, the Helmholtz free energy functional can be formulated as

$$\mathcal{F}(T, [\phi(\boldsymbol{r})]) = \mathcal{F}(T, [\phi(\boldsymbol{r})])_{id} + \mathcal{F}(T, [\phi(\boldsymbol{r})])_{exc} \tag{2}$$

where $\mathcal{F}(T, [\phi(\boldsymbol{r})])_{id}$ is the intrinsic free energy that do not depend on particle interaction and where $\mathcal{F}(T, [\phi(\boldsymbol{r})])_{exc}$ is the excess energy due to particle interaction. Additional contributions can be envisaged in eq. (2), for example due to external potentials, but that is beyond the present scope. The variation of the non-interacting component $\mathcal{F}(T, [\phi(\boldsymbol{r})])_{id}$ can be found for an ideal gas as

$$\Delta\mathcal{F}(T, [\phi(\boldsymbol{r})])_{id} = \rho_0 k_B T \int \left\{ [1 + \phi(\boldsymbol{r})] \ln\left[1 + \phi(\boldsymbol{r})\right] - \phi(\boldsymbol{r}) \right\} d\boldsymbol{r} \tag{3}$$

with k_B denoting the Boltzmann constant. Following the Ramakrishnan-Yussouff pertubation theory usually employed in DFT, cf. [44], the variation of the excess free energy component due to interaction between particles positioned at coordinates $\boldsymbol{r}_1$ and $\boldsymbol{r}_2$ can be formulated as

$$\Delta \mathcal{F}(T, [\phi(\boldsymbol{r})])_{exc} = -\rho_0 \frac{k_B T}{2} \int \phi(\boldsymbol{r}_1) d\boldsymbol{r}_1 \int [C_2(r) \phi(\boldsymbol{r}_2)] \, d\boldsymbol{r}_2 \tag{4}$$

where $C_2(r)$ is the direct pair correlation function and $r = |\boldsymbol{r}_1 - \boldsymbol{r}_2|$. It is this correlation function that permits the formation of periodic structures in PFC and as discussed in [24], different modes can be incorporated into $C_2(r)$ in reciprocal lattice space to achieve a particular crystal structure. This aspect is discussed further below. It can also be noted that higher order correlation functions may be added to eq. (4) to realize more complex crystal structures, but at the expense of an increased computational cost.

Following [13], and under the assumption of a locally conserved density field, the chemical potential of the system can be identified as

$$\mu(\phi(\boldsymbol{r})) = \frac{\delta \mathcal{F}[\phi(\boldsymbol{r})]}{\delta \phi(\boldsymbol{r})} \tag{5}$$

Note that as the temperature is assumed to be constant in what follows, the explicit dependence on T is omitted from here on. Introducing the flux $\boldsymbol{J} = -M \nabla \cdot \mu$, with M being a mobility coefficient, mass conservation requires that

$$\frac{\partial \phi(\boldsymbol{r})}{\partial t} = -\nabla \cdot \boldsymbol{J} \tag{6}$$

where t denotes the time. Eq. (6) provides the Cahn-Hilliard evolution equation for the locally conserved field ϕ as

$$\frac{\partial \phi(\boldsymbol{r})}{\partial t} = M \nabla^2 \mu(\phi(\boldsymbol{r})) \tag{7}$$

A compact and quite general PFC formulation, akin to the format used in [4], can be obtained by formulating the Helmholtz free energy functional as

$$\mathcal{F}[\phi(\boldsymbol{r})] = \int_V \left(\frac{1}{2} \phi(\boldsymbol{r}) \mathcal{D}_i \phi(\boldsymbol{r}) + \frac{g}{4} \phi(\boldsymbol{r})^4 \right) d\boldsymbol{r} \tag{8}$$

Different PFC formulations are obtained from eq. (8) by defining the nonlinear operator $\mathcal{D}_i$, being a rotation-invariant Hamiltonian, as

$$\mathcal{D}_i = \begin{cases} \alpha + \lambda \left(q_0^2 + \nabla^2 \right)^2 & \text{one-mode model}, i = 1 \\ \alpha + \left[r_0 + \lambda \left(q_0^2 + \nabla^2 \right)^2 \right] \left[r_1 + \left(q_1^2 + \nabla^2 \right)^2 \right] & \text{two-mode model}, i = 2 \end{cases} \tag{9}$$

The general formulation in eqs. (8)-(9) encompasses both the original one-mode PFC model introduced in [17, 18] (for $i = 1$), as well as the two-mode model introduced in [60] and later modified in [6] (for $i = 2$). The format in eq. (8) is arrived at by expanding the non-interacting free energy component in eq. (3) as a power series to fourth order. One-mode PFC approximations only utilize the first set of reciprocal lattice vectors (RLV) in the correlation function $C_2(r)$ which limits the types of crystal structures that can be represented to triangular in 2D and BCC in 3D. In [60] it was shown that if the first two sets of RLV are included, also square and FCC crystals can be described in 2D and 3D, respectively. In [39], it was proposed that use

of the first three RLV is sufficient to describe the full range of Bravais lattices. In the present study, which focuses on FCC crystals, a two-mode model is employed corresponding to $i = 2$ in eq. (9).

Appearing in eq. (9), the parameters q_0 and q_1 represent the wave lengths of the first and second density waves while r_0 and r_1 are related to the Fourier amplitudes of the same two density waves. These quantities are further detailed below. In particular, q_0 is the wave number that determines the lattice parameter $a = 2\pi/q_0$ of the crystal and hence the spacing between lattice planes. The additional parameters λ and g in eq. (9) must be identified for any particular material.

For convenience, the PFC formulation can be cast on non-dimensional form by introducing the parameter set

$$\varepsilon = -\frac{\alpha}{\lambda q_0^4}, \quad \psi = \phi\sqrt{\frac{g}{\lambda q_0^4}}, \quad \boldsymbol{x} = q_0\boldsymbol{r}, \quad F = \frac{g}{\lambda^2 q_0^5}\mathcal{F}, \quad \tau = tM\lambda q_0^6 \tag{10}$$

for the one-mode model ($i = 1$) or

$$\varepsilon = -\frac{\alpha}{\lambda q_0^8}, \quad \psi = \phi\sqrt{\frac{g}{\lambda q_0^8}}, \quad R_0 = \frac{r_0}{q_0^4}, \qquad R_1 = \frac{r_1}{q_0^4}, \quad Q_1 = \frac{q_1}{q_0},$$

$$\boldsymbol{x} = q_0\boldsymbol{r}, \qquad F = \frac{g}{\lambda^2 q_0^{13}}\mathcal{F}, \quad \tau = tM\lambda q_0^7 \tag{11}$$

for the two-mode formulation ($i = 2$). Based on the non-dimensional parameters, the time evolution of the locally conserved density field ψ is obtained as

$$\frac{\partial\psi(\boldsymbol{x})}{\partial\tau} = \nabla^2\frac{\delta F[\psi(\boldsymbol{x})]}{\delta\psi(\boldsymbol{x})} \tag{12}$$

where the non-dimensional free energy appears as

$$F[\psi(\boldsymbol{x})] = \int_V \left(\frac{1}{2}\psi(\boldsymbol{x})D_i\psi(\boldsymbol{x}) + \frac{1}{4}\psi(\boldsymbol{x})^4\right)d\boldsymbol{x} \tag{13}$$

with the differential operator D_i being defined by

$$D_i = \begin{cases} -\varepsilon + \left(1 + \nabla^2\right)^2 & \text{one-mode model}, i = 1 \\ -\varepsilon + \left[R_0 + \left(1 + \nabla^2\right)^2\right]\left[R_1 + \left(Q_1^2 + \nabla^2\right)^2\right] & \text{two-mode model}, i = 2 \end{cases} \tag{14}$$

As in DFT, the density in the crystalline state can be formulated based on density waves in terms of RLV $\boldsymbol{k}$ according to

$$\psi = \psi_s + \sum_j A_j e^{i\boldsymbol{k}_j t} \tag{15}$$

where ψ_s is the average dimensionless density in the solid state, i is the imaginary number and A_j is the amplitude in Fourier space of the RLV $\boldsymbol{k}_j$. Further, following [60] the set of RLV are chosen as $\boldsymbol{k}_{111}$ and $\boldsymbol{k}_{200}$, corresponding to the [111] and [200] wave vectors, respectively. This means that the wave lengths $q_0 = |\boldsymbol{k}_{111}|$ and $q_1 = |\boldsymbol{k}_{200}|$ can be identified. This also provides the parameter Q_1, introduced in eq. (11), as $Q_1 = q_1/q_0 = \sqrt{4/3}$ for FCC crystals. Following [60], $\varepsilon = 0.0082$ and $\psi_s = -0.06$ are chosen to ensure a stable solid FCC phase. In fact, ε and ψ_s are the only free parameters in the present non-dimensional study.

If A_s and B_s denote the amplitude in Fourier space of the first and second RLV, respectively, eq. (15) permits the FCC solid state density field to be expressed by the expansion

$$\psi_{FCC} \approx \psi_s + 8A_s \cos(qx)\cos(qy)\cos(qz) + 2B_s\left[\cos(2qx) + \cos(2qy) + \cos(2qz)\right] \quad (16)$$

where $q = 1/\sqrt{3}$. The amplitudes A_s and B_s can be found by inserting eq. (16) into eq. (13) and then minimizing the free energy with respect to A_s and B_s, respectively. This provides a set of two coupled nonlinear equations that can be solved using an iterative scheme, as noted in [8]. With the adopted values for ε and ψ_s, the amplitudes are found as $A_s = 1.30479 \times 10^{-2}$ and $B_s = 9.99079 \times 10^{-3}$, respectively. Following [6], it is also noted that $R_0 = R_1 (B_s/A_s)^2$. In the present case, however, $R_0 = R_1 = 0$ as also considered in [8, 60].

2.1 Numerical implementation

As materials of FCC structure are in focus of the present work, the two-mode formulation provided by eqs. (12)–(14) is considered by setting $i = 2$. This yields the equation of motion for the non-dimensional and locally conserved density field ψ as

$$\frac{\partial \psi(\boldsymbol{x})}{\partial \tau} = \mathcal{L}\psi + h(\psi) \quad (17)$$

where the linear operator $\mathcal{L}$ and the non-linear function $h(\psi)$ were introduced as

$$\mathcal{L} = \nabla^2 \left(c_0 + c_2\nabla^2 + c_4\nabla^4 + c_6\nabla^6 + \nabla^8\right) \quad \text{and} \quad h(\psi) = \nabla^2\psi^3 \quad (18)$$

and where the following constants were defined for the sake of convenient notation

$$\begin{aligned}
c_0 &= R_1(R_0 + 1) + Q_1^4(R_0 + 1) - \varepsilon \\
c_2 &= 2\left(R_0 Q_1^2 + R_1 + Q_1^2 + Q_1^4\right) \\
c_4 &= 1 + R_0 + R_1 + 4Q_1^2 + Q_1^4 \\
c_6 &= 2\left(1 + Q_1^2\right)
\end{aligned} \quad (19)$$

The PFC equation of motion in eq. (17) can be solved using different approaches, for example by finite element or finite difference approximations. Issues might arise, however, when addressing the higher-order derivatives in the operator $\mathcal{L}$ in eq. (18) by such methods. Alternatively, by considering periodic solution domains, eq. (17) be efficiently solved using a semi-implicit spectral algorithm, as discussed in for example [16, 37, 62]. Letting $\widetilde{\mathcal{L}}_{\boldsymbol{k}}$ and $\widetilde{h}_{\boldsymbol{k}}$ denote the Fourier transforms of $\mathcal{L}$ and h, respectively, permits writing the semi-implicit spectral scheme introduced in [37] as

$$\widetilde{\psi}_{\boldsymbol{k}}^{n+1} = e^{\Delta\tau\widetilde{\mathcal{L}}_{\boldsymbol{k}}}\widetilde{\psi}_{\boldsymbol{k}}^n + \frac{\widetilde{h}_{\boldsymbol{k}}}{\widetilde{\mathcal{L}}_{\boldsymbol{k}}}\left(e^{\Delta\tau\widetilde{\mathcal{L}}_{\boldsymbol{k}}} - 1\right) + \frac{\widetilde{h}_{\boldsymbol{k}}^n - \widetilde{h}_{\boldsymbol{k}}^{n-1}}{\Delta\tau\widetilde{\mathcal{L}}_{\boldsymbol{k}}^2}\left(e^{\Delta\tau\widetilde{\mathcal{L}}_{\boldsymbol{k}}} - 1 - \Delta\tau\widetilde{\mathcal{L}}_{\boldsymbol{k}}\right) \quad (20)$$

where $\widetilde{\psi}_{\boldsymbol{k}}$ is the Fourier transform of ψ and where two subsequent steps, indicated by superscripts n and $n + 1$, are separated by the non-dimensional time increment $\Delta\tau$.

The scheme in eq. (20) is adopted in the present work and implemented in CUDA Fortran to take advantage of GPU parallelization and the NVIDIA cuFFT library for fast Fourier transforms.

Grain boundary regions
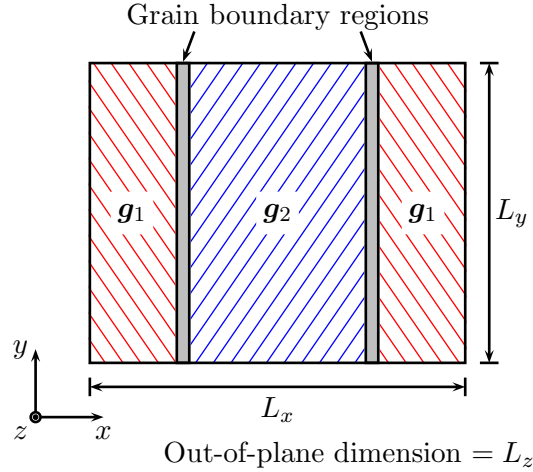
Figure 1: *Schematic illustration of the simulation model setup used for the 3D PFC simulations of grain boundaries in the present work. Two crystals, with orientations $\boldsymbol{g}_1$ and $\boldsymbol{g}_2$, are present in the domain which is modeled as periodic in all three coordinate directions. Due to the periodicity, two identical grain boundaries are present in the model and the grain boundary regions are initially defined as narrow liquid domains without structure. Over the course of each simulation, the adjacent crystals grow into the liquid regions to eventually form the different grain boundary structures, driven by a minimization of the system's energy. This is illustrated in Fig. 2.*

## 3 Energy, structure and stiffness of grain boundaries in FCC materials

Details on the formulation of the PFC simulation model are discussed in subsection 3.1, followed by subsection 3.2 that gives an account for the evaluation of grain boundary energy from the simulations. Subsection 3.3 discusses the prediction of grain boundary structure, obtained from the PFC simulations, followed by Subsection 3.4 that proposes a methodology for evaluating grain boundary stiffness from the PFC density field, based on grain boundary fluctuations.

3.1 Simulation setup

The grain boundary simulations are based on 3D PFC models and are set up as schematically illustrated in Fig. 1. The 3D domain is assumed to be periodic in all coordinate directions and two crystals, with orientations $\boldsymbol{g}_1$ and $\boldsymbol{g}_2$, are present in the domain. Due to the periodicity, two identical grain boundaries are present, with normal directions parallel to the x-axis. The crystal structure is initiated using the density field provided by eq. (16) with rotations applied to provide different grain boundary types. The grain boundaries are initiated as narrow liquid regions and over the course of the simulations, driven by minimization of the free energy functional, the crystals grow into these regions and form the grain boundary structure. This process is illustrated in Fig. 2.

To ensure that periodicity of the density field is satisfied between opposite domain boundaries, the scheme introduced in [37] for a 2D hexagonal crystal structure is adopted here and recast to suit the present 3D FCC conditions.

By this approach, base vectors are defined along the coordinate axes in terms of the non-dimensional lattice parameter $a = 2\pi/q_0$. These base vectors will depend on the crystal orientation and the corresponding spacing between density peaks along each coordinate direction for

a)   b)   c)
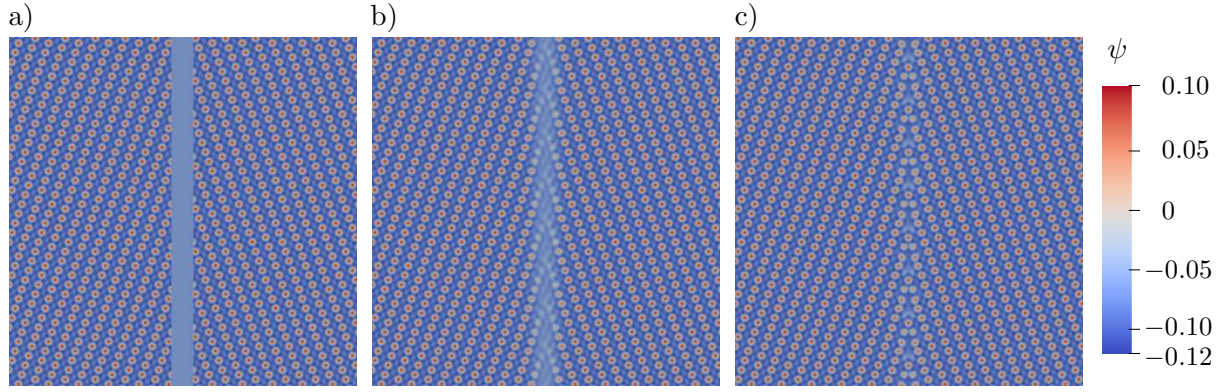
Figure 2: *Three stages of the density field evolution in an initially liquid grain boundary region, cf. Fig. 1, during a PFC simulation of a $\Sigma 9$ (114) symmetrical tilt grain boundary with [110] tilt axis. Note that only a small region of the full simulation domain is shown. a) Initial state, b) intermediate state and c) final state.*

each boundary type, as summarized in Table 1. Consider, as an example, the case of a symmetrical [110] tilt grain boundary. Following Table 1, the spacing between density peaks along the z-direction is used to directly define the dimension $L_z = a/\sqrt{2}$, with L_z subsequently being held constant in all simulations involving this tilt axis. Two base vectors $\boldsymbol{a}$ and $\boldsymbol{b}$ are defined along the x- and y-axes, respectively, as $\boldsymbol{a} = a\,[1\ 0]^T$ and $\boldsymbol{b} = a/\sqrt{2}\,[0\ 1]^T$, with $(\cdot)^T$ denoting a transpose. These base vectors are rotated into $\boldsymbol{a}_{rot}$ and $\boldsymbol{b}_{rot}$ in the next step, to account for the tilt angle θ, whereby

$$\boldsymbol{a}_{rot} = \boldsymbol{R}^T \boldsymbol{a} \quad \text{and} \quad \boldsymbol{b}_{rot} = \boldsymbol{R}^T \boldsymbol{b} \tag{21}$$

with $\boldsymbol{R}$ being the 2×2 orthogonal rotation matrix defining a rotation around the z-axis through an angle θ. When forming a symmetrical tilt boundary, the orientations $\boldsymbol{g}_1$ and $\boldsymbol{g}_2$, shown in Fig. 1, are defined by a rotation of $\theta/2$ in opposite directions for the two crystals. In a periodic system, the domain dimension along each coordinate direction must correspond to an integer number of steps along each base vector. This can be used to combine the rotated base vectors into the vector equations

$$
\begin{aligned}
i\boldsymbol{a}_{rot} + j\boldsymbol{b}_{rot} &= \left[\begin{array}{c} L_x \\ 0 \end{array}\right] \\
-k\boldsymbol{a}_{rot} + l\boldsymbol{b}_{rot} &= \left[\begin{array}{c} 0 \\ L_y \end{array}\right]
\end{aligned}
\tag{22}
$$

where i, j, k, l are integer numbers. Following [37], the signs on the left-hand side of eq. (22) are

Table 1: *Crystal orientations and density peak spacing along each coordinate direction used when setting up the periodic simulation domain for the different types of symmetrical tilt grain boundaries under consideration. The initial crystal orientation $\boldsymbol{g}$ is rotated to provide the two crystals orientations $\boldsymbol{g}_1$ and $\boldsymbol{g}_2$ illustrated in Fig. 1.*

Tilt axis	Initial crystal orientation $\boldsymbol{g}$	Density peak spacing along (x, y, z)
[100]	$(100)//x$, $(010)//y$, $(001)//z$	(a, a, a)
[110]	$(1\bar{1}0)//x$, $(001)//y$, $(110)//z$	$(a\frac{1}{\sqrt{2}}, a, a\frac{1}{\sqrt{2}})$
[111]	$(\bar{1}10)//x$, $(\bar{1}\bar{1}2)//y$, $(111)//z$	$(a\frac{1}{\sqrt{2}}, a\sqrt{\frac{3}{2}}, a\sqrt{3})$

chosen to provide positive integers. Using the equations in eq. (22) with a zero on the right-hand side, results in two conditions on the angle θ according to

$$\tan \theta = \frac{j}{i\sqrt{2}} \quad \text{and} \quad \tan \theta = \frac{k\sqrt{2}}{l} \tag{23}$$

Periodic simulation domains can only be defined for sets of the integers i, j, k, l which satisfy these two conditions. Once identified, the integers can be used in the two equations in eq. (22) with non-zero right-hand sides to obtain the domain dimensions in the x- and y-directions as

$$
\begin{aligned}
L_x &= a\left[i\cos\theta + \frac{j}{\sqrt{2}}\sin\theta\right] \\
L_y &= a\left[k\sin\theta + \frac{l}{\sqrt{2}}\cos\theta\right]
\end{aligned}
\tag{24}
$$

For other boundary types and crystal orientations the base vectors $\boldsymbol{a}$ and $\boldsymbol{b}$ must be chosen differently, as indicated by Table 1, but the procedure in eqs. (21)–(24) is the same.

As a result of the periodicity requirement and the obtained domain dimensions, the grid spacing cannot in general be held equal in different coordinate directions. The number of grid points along each axis is, however, chosen to meet a target grid spacing of $\Delta x = \Delta y = \Delta z = \pi/4$ as this grid spacing has been found to work well in PFC implementations employing spectral solution schemes [17, 18, 37]. The obtained values of L_x, L_y and L_z provide the minimum dimensions to maintain a periodic simulation domain. In the present case, however, the values are multiplied by integer values to expand the domain along the x- and y-directions in order to mitigate any influence of the domain size, especially from the spacing between the periodic grain boundaries, on the resulting grain boundary energy. This is discussed in further detail in subsection 3.2.

A typical simulation domain is in the present work discretized by approximately 30×10^6 grid points and contains in the order of 25×10^3 atoms (density peaks). Different non-dimensional time increments Δt were evaluated and it was found that $\Delta \tau = 1$ provides stable results. In fact, a unit time increment appears as a conservative choice as also two or three times this value gives negligible differences in the simulation results. The simulations are ran until the relative change over 25 time steps in the average free energy density of the system is below 10^{-10}. This choice of termination criteria ensures that each grain boundary structure has obtained its (numerically) stagnant low energy configuration before stopping. A typical simulation requires approximately 30-60 minutes when running the current 3D GPU implementation with this quite restrictive termination criteria. Numerical experiments were performed, however, indicating that the resulting grain boundary energies and structures are quite unaffected when relaxing the termination criteria by increasing it by one or two orders of magnitude, allowing the simulation times to be reduced with only negligible variations in the resulting grain boundary energy and structure.

3.2   Grain boundary energy

The grain boundary energy γ_{gb} can be evaluated from the PFC simulations by comparing the free energy f_{gb} of a simulation domain which contains a grain boundary, to the free energy f_0 of a domain containing a perfect crystal without grain boundaries. This provides the grain boundary energy as

$$\gamma_{gb} = L_x \frac{f_{gb} - f_0}{2} \tag{25}$$
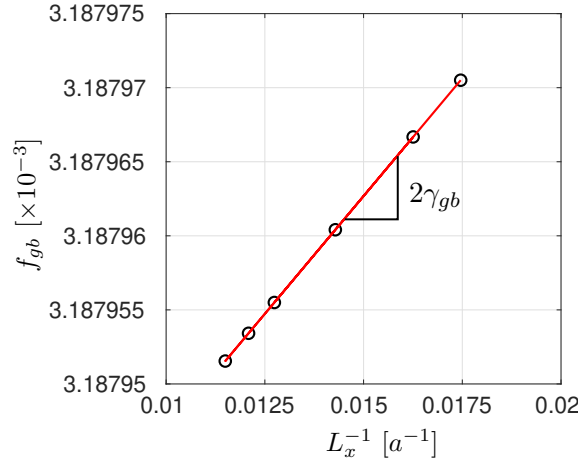
Figure 3: *Average free energy density in the simulation domain as function of the inverse of the domain size L_x along an axis perpendicular to the grain boundary, cf. Fig. 1. The results are taken from the present PFC simulations of a $\Sigma 9$ (114) symmetrical tilt grain boundary with [110] tilt axis. Non-dimensional quantities are plotted. The open circles show simulation data and the solid line the fit of a linear function according to eq. (26). The slope of the line provides the grain boundary energy, multiplied by a factor of two due to the presence of two grain boundaries in the periodic simulation domain.*

where the domain size L_x is present to provide the correct dimensions and where the factor $1/2$ is due to the presence of two grain boundaries in the periodic domain. There are, however, numerical issues related to this direct approach which relate to the very small energy differences that must be handled and possibly also to numerical errors present in the evaluation of gradients in the free energy, as noted in [32, 37]. In [37], a more stable approach is introduced based on reformulating eq. (25) to express f_{gb} as a function of L_x^{-1} according to

$$f_{gb} = 2\gamma_{gb}L_x^{-1} + f_0 \qquad (26)$$

In the absence of numerical errors, a plot of f_{gb} versus L_x^{-1} will be a straight line and the grain boundary energy γ_{gb} can evaluated as $1/2$ of the slope of the linear function. This is illustrated in Fig. 3, where the symbols show the present PFC results for a $\Sigma 9$ (114) symmetrical tilt grain boundary with a [110] tilt axis. The solid line is a fitted linear function, indicating that the PFC data is well represented by a linear function as given by eq. (26). All grain boundary energies presented in the present work are based on four or more simulations with different domain sizes L_x. The results were in all cases well represented by a linear fit, as in Fig. 3, indicating negligible numerical errors in the evaluation [37].

The study performed herein is based on a non-dimensional formulation of the PFC model, as discussed in Section 2. By purpose, the model is not fitted to a particular FCC material in order to maintain generality. It can be noted, however, that the PFC model parameters can be set to fit individual materials as shown for Ni and Al in [8] and for Ni in [60]. Employing a non-dimensional model is further motivated by the MD study in [51], showing the transferability of grain boundary energy data from one FCC system to another by scaling. Such a correspondence between different materials is also demonstrated by the extensive grain boundary energy data sets obtained for Al and Ni by MD simulations in [42]. The latter study gives a strong indication that the grain boundary energy in different materials of FCC structure will have approximately
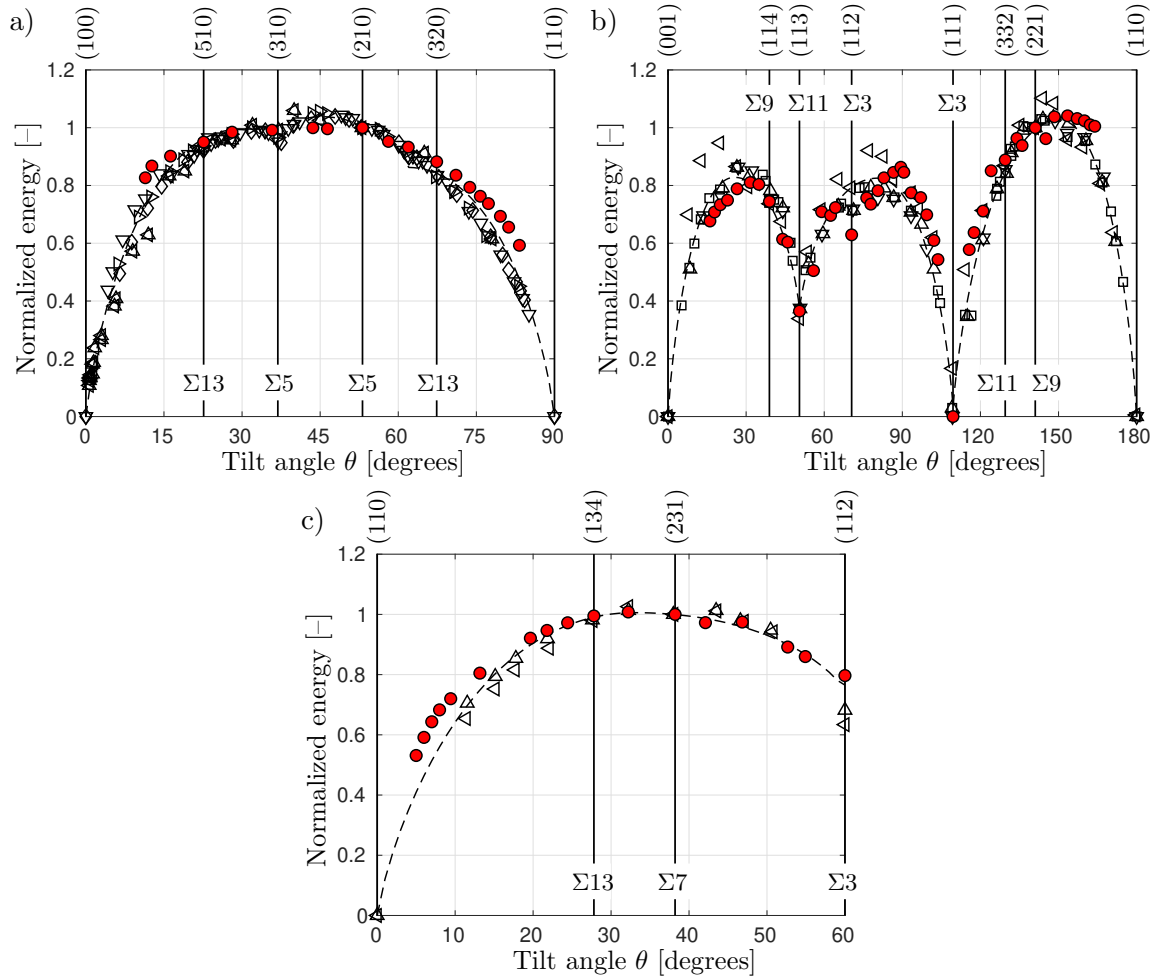
Figure 4: *Energy of symmetric tilt grain boundaries obtained by the present PFC simulations (red filled circles) compared to energy data taken from the literature. Dashed lines show the energy variations obtained using the GB5DOF code in [12]. Special grain boundary configurations (Σ-type boundaries) are indicated by vertical lines, labeled with the boundary plane normal direction above the plots. a) Energy of tilt boundaries with a [100] misorientation axis, normalized by the energy of the Σ5 (210) boundary, with data from [52] (▽), [23] (△ and ◁), [59] (▷) and [51] (◇). b) Energy of tilt boundaries with a [110] misorientation axis, normalized by the energy of the Σ9 (221) boundary, with data from [52] (□), [45] (▽) and [51] (◁ and △). c) Energy of tilt boundaries with a [111] misorientation axis, normalized by the energy of the Σ7 (231) boundary, with data from [59] (◁ and △).*

the same variation with the macroscopic geometric degrees of freedom, only separated by a material-specific scaling factor. The same behavior can be seen in Fig. 4 where grain boundary energy data for FCC materials has been compiled from various sources, showing a high level of agreement between the data sets.

The grain boundary energy variation will to some extent be influenced by the temperature. As an example, a decreasing temperature can be expected to make the energy cusps wider and more shallow [38, 47]. In the present non-dimensional PFC implementation the temperature is only present in terms of the parameter ε. The value $\varepsilon = 0.0082$ is adopted from the study in [60] wherein it is noted that this places the system close to the melting point but well into the solid FCC region of the phase diagram. This may have an impact on the appearance of the variation of the grain boundary energies in Fig. 4. But as also the other data sets in Fig. 4 – obtained from the literature and used for comparison – are obtained at quite varying temperatures, we tacitly assume the energy variations to be representative for FCC-structured materials.

A total of 80 different [100], [111] and [110] symmetrical tilt grain boundaries (STGB) have been evaluated by PFC in the present study and the filled red circles in Fig. 4 show the predicted grain boundary energies. Which tilt angles θ are investigated for each tilt axis is determined by the requirement of maintaining a periodic simulation domain, as discussed in Section 3.1.

Fig. 4a shows the energy variation of [100] STGB with the individual data sets normalized by the energy of the $\Sigma 5$ (210) grain boundary at $53.1°$. The grain boundary energy predictions from the PFC simulations are seen to fairly well capture the energy variations observed in the other data sets.

Fig. 4b shows the energy of [110] STGB, normalized by the energy of the $\Sigma 9$ (221) boundary at $141.1°$. The PFC data is seen to systematically predict slightly lower energy values for tilt angles below approximately $30°$. There is also a tendency for overestimating the energy around $\theta = 90°$. This tendency is, however, shared with the MD-based results taken from [51].

The energy variation of [111] STGB is shown in Fig. 4c and it can be noted that the PFC results are in good agreement with the other data sets, although the PFC data appears to predict slightly higher energies for low-angle boundaries at $\theta < 15°$. Misorientations are only shown up to $60°$ as the misorientations θ and $120° - \theta$ for [111] STGB are identical in FCC crystals [49]. For the $\Sigma 3$ (112) boundary, the PFC energy is almost identical to the energy predicted by the GB5DOF model in [12] (shown by a dashed line in the plots in Fig. 4), while the two data points from [59] for the same boundary, obtained from MD simulations, predict slightly lower energy values.

3.3 Grain boundary structure

In order to further verify the predictions provided by the PFC simulations, the structure of the grain boundaries can be considered in addition to the grain boundary energies discussed in Section 3.2. To evaluate grain boundary structure, it is convenient to have access to the positions of individual atoms, as provided by MD simulations. But while MD consider discrete atoms or particles, PFC is based on the evaluation of a continuous density field, cf. Section 2. To address this, a quadratic interpolation of the density field is performed in 3D to locate the density maxima, corresponding to the "atoms" in the simulated crystal structure. A similar approach is also adopted in, for example, [61]. Fig. 5a shows a part of the density field obtained from the PFC simulation of a $\Sigma 11$ (332) grain boundary with [110] tilt axis. Fig. 5b shows the
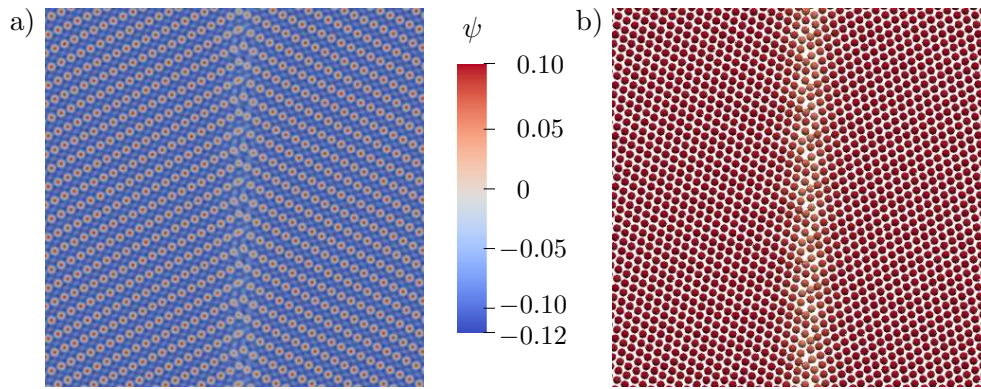
Figure 5: *a) PFC density field for the [110] Σ11 (332) grain boundary (note that only a part of the simulation domain is shown). b) Density maxima, corresponding to atom positions, interpolated from the domain in figure a. The color legend is common to both a and b.*

interpolated density field maxima, corresponding to the atom positions, of the same region.

As seen in Fig. 5a, the density field will exhibit incomplete maxima along a general grain boundary, except for along fully coherent twin boundaries. This means that a selection among the identified maxima may be required to distinguish actual maxima from those which are incomplete and do not represent atom positions. In the present study atoms are identified as those maxima having a density ≥ 75 % of the maximum density in the simulation domain. This was found to be a robust threshold for the present application, but alternative selection criteria can be envisaged. One possibility is to consider the energy field that exhibits minima at the density maxima. Alternatively, the value of a phase field – as discussed in Section 3.4 – at the interpolated density maxima can be used. Yet another possibility is to use the identified maxima to evaluate quantities such as the centrosymmetry parameter, introduced in [33] and often used in MD simulations, to distinguish between the density maxima. A somewhat different approach is offered by employing the "Vacancy PFC" (VPFC) formulation, proposed in [14]. In VPFC, an additional term is added ot the free energy in eq. (13) to penalize negative values in the density field whereby voids or vacancies are represented by near-zero values of the density. This can be used to only maintain those density maxima that correspond to actual atom positions.

The atom configuration along a number of representative grain boundaries considered in the present study is shown in Fig. 6. Atoms in the top layer, facing the reader, are indicated by filled (red) circles and atoms in the layer beneath are indicated by filled (blue) squares. In order to verify that realistic grain boundary configurations are obtained from the PFC simulations, the idea of "structural units" (SU) can be employed. The SU concept is usually attributed to [10] and has been further evolved in, for example, [49]. The idea behind the SU concept is that a grain boundary can be represented by a repeated arrangement of structural (geometrical) units that connect the interface atoms of the two abutting crystals. Solid lines have been drawn in Fig. 6 to indicate the sequential arrangement of structural units along the individual grain boundaries and to give a qualitative indication that the PFC model predicts the expected grain boundary structures.

Fig. 6a-d depicts a number of [100] STGB where the characteristic kite-like SU's are seen, in agreement with the [100] boundaries investigated in, for example, [43, 53].

Fig. 6e-g show [111] STGB configurations obtained from the PFC simulations. These structures are in agreement with those found in [15, 57]. It can be noted, however, that these two
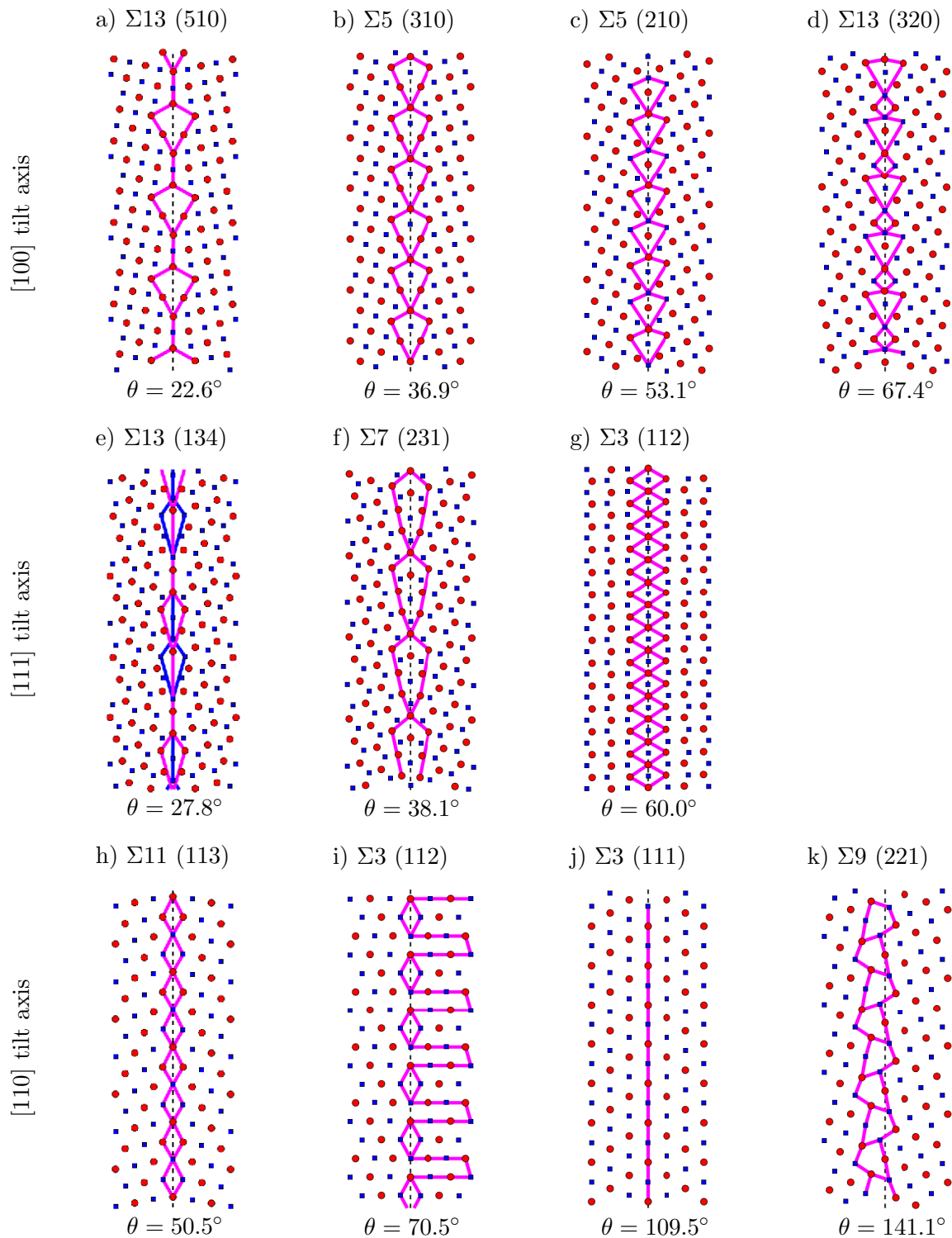
Figure 6: *Grain boundary structures obtained from the PFC simulations for three different tilt axes: a-d) [100], e-g) [110] and h-k) [111]. Different symbols (red circles and blue squares) indicate atoms in two different layers along the tilt axis. The CSL number Σ, the grain boundary plane normal (hkl) and the tilt angle θ is provided at each figure.*

sources give alternative SU representations of the [111] $\Sigma13$ (134) grain boundary. SU at two different atom layers along this grain boundary are indicated by solid lines of different color in Fig. 6e.

Fig. 6h-k show the structure of STGB with a [110] tilt axis. The high symmetry of the coherent $\Sigma3$ (111) twin boundary in Fig. 6j can be noted. The [110] STGB structures are in agreement with previous studies, for example those found in [15, 52, 64]. A slight discrepancy is seen in Fig. 6i where the PFC simulations predict a more straightened grain boundary profile than expected from the other studies.

3.4 Grain boundary stiffness

Prior to addressing grain boundary stiffness, the issue of identifying the grain boundary shape is considered by finding the boundary as a sharp interface between the adjacent crystals. This is achieved by constructing a continuous phase field throughout the simulation domain by considering the periodic nature of the PFC solution and evaluating the corresponding phase field through wavelet filtering. The idea of using continuous wavelet transforms for this purpose was originally proposed in [48] and later adopted for PFC in, for example, [56]. By this approach the lattice orientations are identified from the density field by performing an initial convolution of the density field with a wavelet function w_1 that is sensitive to the lattice structure in question and then, in a subsequent step, smoothing the result by a second convolution using a Gaussian wavelet kernel w_2. The phase field is thus obtained through the repeated convolutions

$$\xi = (\psi * w_1) * w_2 \tag{27}$$

where $*$ denotes a convolution operation. To establish w_1, a rotation-dependent direct pair correlation function can be formulated in Fourier space, following [25], as

$$\widetilde{C}_{2,i}(\boldsymbol{k}) = \exp\left(-\frac{|\boldsymbol{k} - \boldsymbol{k}_i|^2}{2\sigma_1^2}\right) \tag{28}$$

where $\boldsymbol{k}$ is the wave vector introduced in Section 2, $\boldsymbol{k}_i$ is the vector related to mode i in reciprocal lattice space and σ_1^2 is the variance. As introduced in Section 2, it is recalled that $\widetilde{(\cdot)}$ denotes a quantity in Fourier space. Considering all modes i, the maximum value of the direct pair correlation in eq. (28) is used as the wavelet w_1 for the initial transform (in Fourier space) by setting

$$\widetilde{w}_1(\boldsymbol{k}) = \max_i\left(\widetilde{C}_{2,i}(\boldsymbol{k})\right) \tag{29}$$

Since FCC crystals are in focus here, the modes i comprise the $\boldsymbol{k}_{111}$ and $\boldsymbol{k}_{200}$ vectors as noted in Section 3.1. The second wavelet is taken as the Gaussian smoothing kernel

$$\widetilde{w}_2(\boldsymbol{k}) = \frac{1}{\sigma_2\sqrt{2}}\exp\left(-\frac{\boldsymbol{k}^2}{2\sigma_2^2}\right) \tag{30}$$

where the variance σ_2 sets the width of the smoothing Gaussian. In the present study the variance parameters in eqs. (28) and (30) are set to $\sigma_1 = 0.45$ and $\sigma_2 = 0.25$, respectively. With both wavelet kernels $\widetilde{w}_1$ and $\widetilde{w}_2$ defined in Fourier space, as well as the density field $\widetilde{\psi}_{\boldsymbol{k}}$, the convolution operations in eq. (27) reduce to straightforward multiplications.
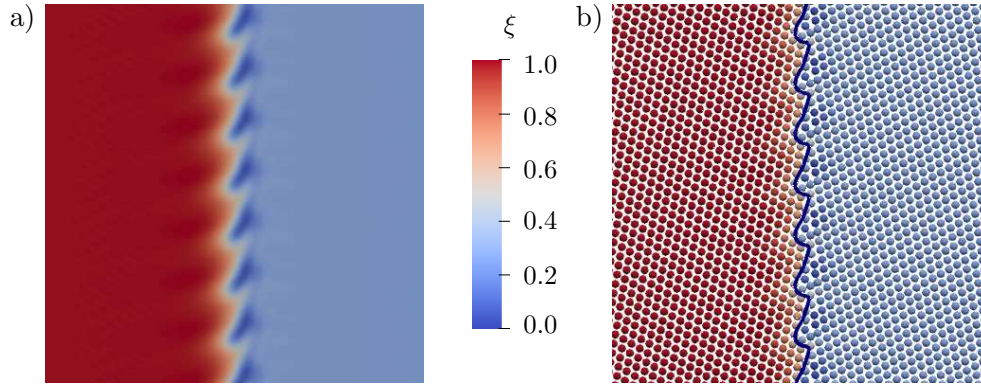
Figure 7: *a) The phase field ξ, evaluated according to eq. (27) and corresponding to the [110] $\Sigma 11$ (332) density field shown in Fig. 5a (note that only a part of the simulation domain is shown). b) Interpolated atoms (density maxima) colored by their ξ value in the region shown in a. The grain boundary found at $\xi = 0.5$ is drawn by a solid black line in b.*
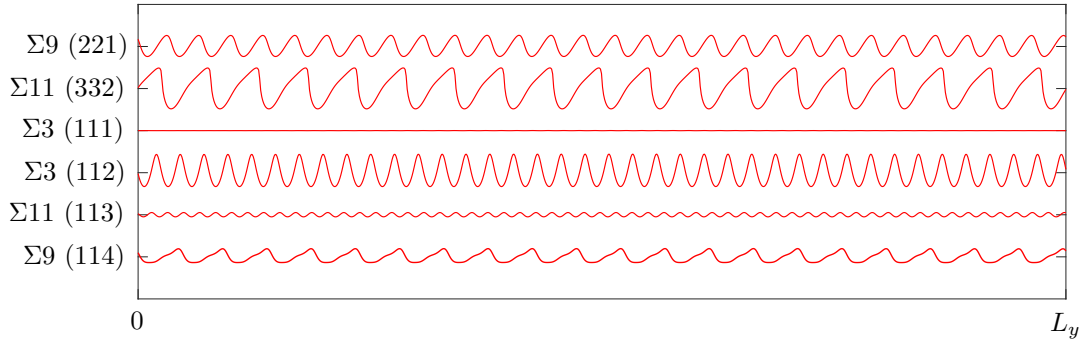
Figure 8: *Grain boundary profiles obtained from the phase field at $\xi = 0.5$ and at coordinate $z = 0$ for a number of STGB with [110] tilt axis. The smooth interface of the coherent $\Sigma 3$ (111) twin boundary can be noted.*

Fig. 7a illustrates the phase field ξ obtained by applying the wavelet filtering in eq. (27) to the density field of the [110] $\Sigma 11$ (332) STGB, shown in Fig. 5a. The phase field in Fig. 7 is normalized such that $\xi \in [0, 1]$. As only two lattice orientations are present in the considered bi-crystal, the individual crystals are clearly distinguishable by the value of ξ and the grain boundary is located around $\xi = 0.5$, as shown by the solid black line in Fig. 7b.

To give an extended view of the variation of grain boundary geometries provided by the present approach, Fig. 8 shows the profiles of a number of STGB with a [110] tilt axis. These profiles are also obtained from the respective phase fields at $\xi = 0.5$ and are drawn at $z = 0$.

As a sharp representation of the grain boundaries is now available, the next step is to consider the accumulated information from the PFC simulations for evaluation of grain boundary stiffness. As a point of departure, it is recalled that grain boundary energy γ_{gb} is a function of five degrees of freedom (DOF), comprising the misorientation θ across the boundary and the normal $\boldsymbol{n}$ of the grain boundary plane [27]. Following the work in [28, 50] and considering curvature-driven grain boundary migration, the local migration velocity of a grain boundary is found as

$$v = M_{gb} \left[\left(\gamma_{gb} + \frac{\partial^2 \gamma_{gb}}{\partial \alpha_1^2} \right) \kappa_1 + \left(\gamma_{gb} + \frac{\partial^2 \gamma_{gb}}{\partial \alpha_2^2} \right) \kappa_2 \right] \tag{31}$$

where M_{gb} is the grain boundary mobility and where $\kappa_{1,2}$ and $\alpha_{1,2}$ denote the principal curvatures

and the related interface inclinations, respectively. The grain boundary stiffness is identified from eq. (31) as

$$\Gamma_{gb}(\theta, \boldsymbol{n}) = \gamma_{gb}(\theta, \boldsymbol{n}) + \gamma_{gb}(\theta, \boldsymbol{n})'' \tag{32}$$

It can be noted that the misorientation θ will be a constant here as the crystal orientations are held fixed for each grain boundary configuration that is studied and the second-derivative in eq. (32) is taken with respect to the boundary inclination. As recently emphasized in [1, 40], the grain boundary stiffness is a key thermodynamic parameter in a range of important grain boundary phenomena, including grain boundary migration, roughening, segregation and grain boundary phase transformations, commonly referred to as grain boundary "complexions". In [29, 50] it is noted that the grain boundary stiffness may vary more due to the boundary plane inclination than the grain boundary energy on misorientation alone. It can also be noted that in numerical mesoscale models involving grain boundary migration – for example those based on phase fields, vertex formulations, cellular automata or level sets, cf. [26] – the inclination dependence of the grain boundary energy is commonly neglected. A main reason for this severe simplification is likely the issue of correctly describing the full five-DOF dependence of the grain boundary energy/stiffness for general grain boundaries.

Based on the work in [11, 58] and as discussed in, for example, [2, 21, 22, 50, 54, 63], the grain boundary stiffness can be seen as a measure of the boundary's resilience towards geometrical changes. Considering the two components of Γ_{gb} in eq. (32), γ_{gb} is the energy related to extension of the boundary and the second derivative γ_{gb}'' is related to the energy involved in a local rotation of the boundary. This is the basis for the "Capillary Fluctuation Method" (CFM), which has been employed in several MD-based studies as a convenient means for determining grain boundary stiffness. An overview of CFM can be found in [29]. If the grain boundary equilibrium profile is represented as a Fourier series

$$S_{gb}(\boldsymbol{r}, t) = \sum_{\boldsymbol{k}} A_{gb}(\boldsymbol{k}) \exp(i\boldsymbol{k} \cdot \boldsymbol{r}) \tag{33}$$

and in the small slope limit $|\nabla_{\boldsymbol{r}} S_{gb}| \ll 1$ – corresponding to the long wavelength limit with wavelengths much larger than the grid spacing – it holds that the grain boundary stiffness is directly related to the equilibrium static fluctuation spectrum of a molecularly rough interface according to

$$\langle |A_{gb}(\boldsymbol{k})|^2 \rangle = \frac{k_B T}{L_y L_z \Gamma_{gb}(\hat{k}) k^2} \tag{34}$$

where L_y and L_z are the dimensions in the plane of the initial flat interface, with coordinates being defined in Fig. 1. Further, k is the magnitude of $\boldsymbol{k}$ and $\hat{k}$ is a unit vector in the direction of $\boldsymbol{k}$. $\Gamma_{gb}(\hat{k})$ is the interface stiffness in the $\hat{k}$-direction.

In MD simulations, $\langle |A_{gb}(\boldsymbol{k})|^2 \rangle$ must in general be evaluated as an average over an extended simulation time due to temporal variations of the interface morphology [22, 29, 50]. This need for averaging of the grain boundary morphology is avoided in PFC as a quasi-static equilibrium ground state configuration of the grain boundary is obtained after sufficient simulation time, as discussed in Section 3.1. The brackets $\langle \cdot \rangle$ that denote an average are, however, kept here as PFC in itself provides an average of fluctuations at very short time scales. The present phase
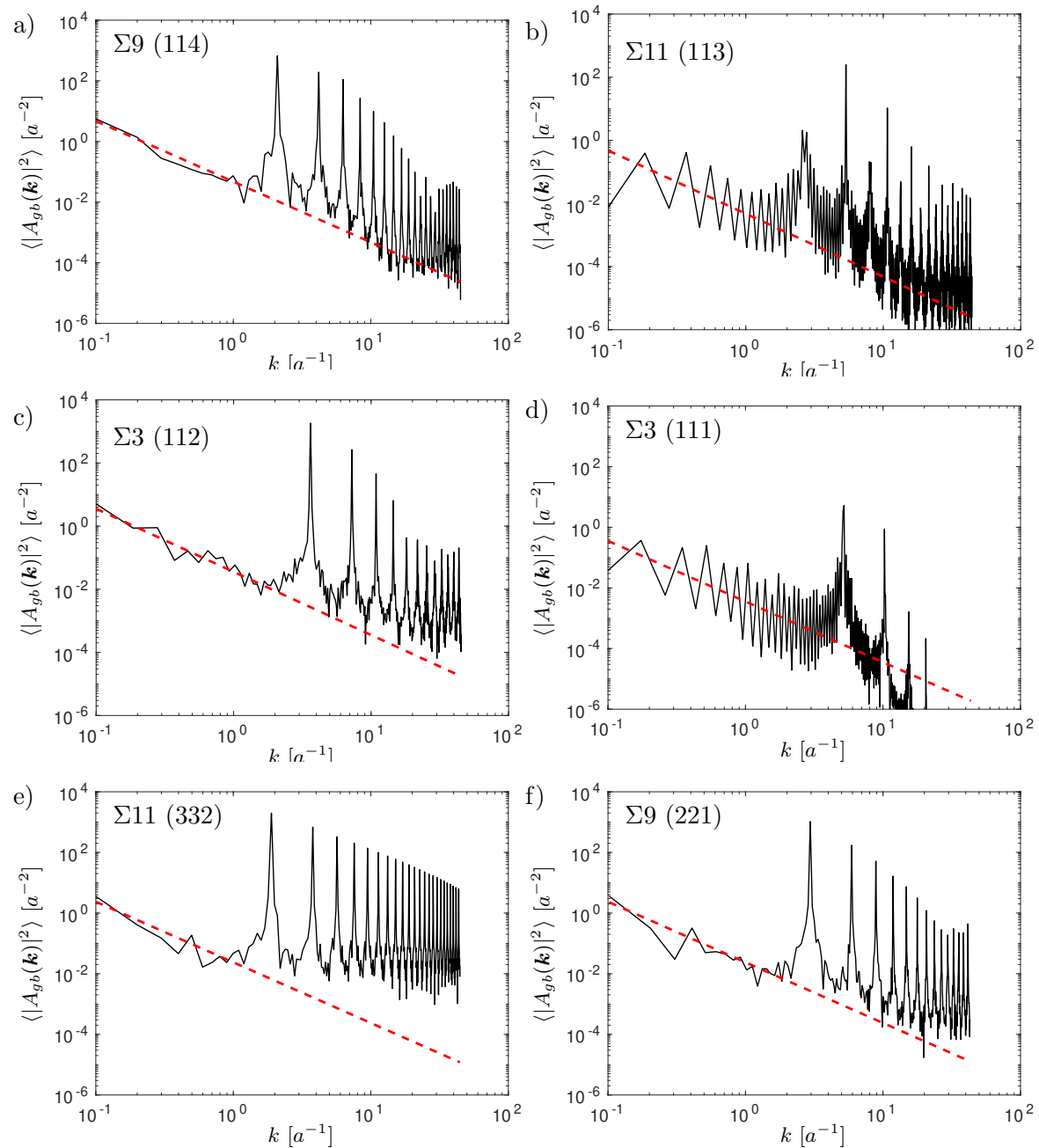
Figure 9: *Power spectra of the equilibrium grain boundary profiles for* [110] *STGB. a)* Σ9 (114), *b)* Σ11 (113), *c)* Σ3 (112), *d)* Σ3 (111), *e)* Σ11 (332) *and f)* Σ9 (221). *The dashed red lines have a slope of* −2 *and are in each figure vertically offset to fit the long wavelength region, identified at values of* $k <\sim 1.5a^{-1}$.

field-based evaluation of the grain boundary geometry, cf. Fig. 7, also conveniently avoids the range of steps required to identify the grain boundary shape during MD simulations, as discussed in [50].

Power spectra based on the grain boundary profiles in Fig. 8 are shown in Fig. 9. As discussed related to the MD-based studies in [22, 29, 50], the decay of the amplitudes can be expected to be proportional to k^{-2} for rough surfaces in the long wavelength limit, i.e. for small values of k. The same trend is clearly seen in the present PFC-based results in Fig. 9 in which dashed red lines with a slope of -2 have been drawn together with the power spectra. The dashed red lines are offset vertically to fit the long wavelength regime of each spectrum up to $k \leq 1.5a^{-1}$. This corresponds well to the k-range considered in [22, 50]. For shorter wavelengths, i.e. at higher values of k, all the spectra in Fig. 9 exhibit quite sharply defined peaks indicating the presence of dominant modes in the spectral content. The vertical offset of the power spectra in Fig. 2 is a measure of the anisotropy of the grain boundary stiffness [29].

The agreement of the results shown in Fig. 9 with those discussed in, for example, [22, 29, 50] shows that the present PFC-based approach is a viable alternative to CFM based on MD. The use of PFC for evaluation of grain boundary stiffness is further motivated as it avoids computationally demanding time averaging of boundary fluctuations and also the effort involved in a repeated reconstruction of the grain boundary geometry, as called for if using MD.

Having demonstrated that the power spectrum fluctuations $\langle |A_{gb}(\boldsymbol{k})|^2 \rangle$ can be conveniently determined from PFC simulations, means that also the grain boundary stiffness is available by evaluating eq. (34). As noted in the MD-based study in [22], the anisotropy of the grain boundary stiffness can be determined by performing the stiffness evaluation along $\boldsymbol{k}$-vectors in different directions. In [9], it is noted that the evaluation of Γ_{gb} can be done for different orientations of the boundary plane normal $\boldsymbol{n}$, after which an expansion of $\gamma_{gb} = \gamma_{gb}(\boldsymbol{n})$ in terms of cubic harmonics can be used to fit the simulation data. A corresponding fit of a Taylor expansion of the grain boundary energy to MD data is detailed in [1]. Such grain boundary stiffness analysis, based on PFC, will be considered in forthcoming studies. In addition, it can be noted that CFM is also frequently adopted to evaluate the anisotropy of grain boundary mobility M_{gb}, cf. eq. (31), as discussed in for example [22, 36]. Use of PFC for this purpose remains to be investigated further, elaborating on the results presented here.

4 Concluding remarks

The present study investigates the possibilities in using PFC modeling to predict grain boundary properties in FCC-structured materials. This complements existing PFC studies which have almost exclusively focused on 2D lattices or on BCC-structured materials in 3D and which are to a large extent limited to low-angle grain boundaries in such materials. Based on 3D simulations, and using a two-mode PFC model, a large number of symmetrical tilt grain boundaries have been studied in the present work and its is found that both grain boundary energy and grain boundary structure are predicted in very good agreement with comprehensive data sets taken from the literature. In addition, continuous phase fields are evaluated from the PFC results using wavelet transforms. It is shown that this approach makes it possible to estimate sharp interface representations of grain boundaries from the numerical results. This information is then used in a subsequent step to obtain the spectral content of the grain boundary fluctuations, which is

directly proportional to the grain boundary stiffness, being a key thermodynamic parameter in grain boundary mechanics. To the authors' knowledge, this is the first study that explores this methodology based on PFC, as it is usually based on averaging of the output from MD over extended simulation times. The successful application of PFC to evaluation of grain boundary stiffness also paves the way for extended studies into the anisotropy of grain boundary stiffness and also into corresponding variations in grain boundary mobility, based on PFC. Another interesting prospect for future investigation is to use the frequency spectrum of grain boundary profiles as a "fingerprint", identifying individual grain boundaries and permitting categorization of different classes of grain boundaries.

Having verified the applicability of PFC to studies on grain boundary mechanics in FCC-structured materials, new possibilities are available for studying grain boundary evolution with the high spatial resolution provided by PFC, and at time scales not tractable when using MD.

In addition to restrictive time limitations, another issue in performing first principle or MD simulations of grain boundaries arises from the fact that a minimum-energy structure of each grain boundary needs to be sought before running the simulation. This is usually achieved by performing an iterative relaxation procedure during which the positions of individual atoms are gradually adjusted [41], possibly combined with rigid body translations of the abutting crystals and followed by a removal of overlapping atoms. This pre-processing procedure carries a certain degree of uncertainty regarding whether a minimum-energy configuration has actually been found or not. This issue is, however, largely avoided when performing PFC simulations which evolve towards states of minimum energy without the need for the pre-processing steps required in MD.

Acknowledgement

References

[1] F. Abdeljawad, S.M. Foiles, A.P. Moore, A.R. Hinkle, C.M. Barr, N.M. Heckman, K. Hattar, and B.L. Boyce. The role of the interface stiffness tensor on grain boundary dynamics. *Acta Mater.*, 158:440–453, 2018.

[2] D.B. Abraham. Capillary waves and surface tension: An exactly solvable model. *Phys. Rev. Lett.*, 47(8):545–548, 1981.

[3] A. Adland, A. Karma, R. Spatschek, D. Buta, and M. Asta. Phase-field-crystal study of grain boundary premelting and shearing in bcc iron. *Phys. Rev. B*, 87:024110, 2013.

[4] V. Ankudinov and P.K. Galenko. Growth of different faces in a body centered cubic lattice: A case of the phase-field-crystal modeling. *J. Cryst. Growth*, 539:125608, 2020.

[5] A.J. Archer, M.J. Robbins, and U. Thiele. Solidification fronts in supercooled liquids: How rapid fronts can lead to disordered glassy solids. *Phys. Rev. E*, 86:031603, 2012.

[6] E. Asadi and M. Asle Zaeem. A modified two-mode phase-field crystal model applied to face-centered cubic and body-centered cubic orderings. *Comput. Mater. Sci.*, 105:110–113, 2015.

[7] E. Asadi and M. Asle Zaeem. A review of quantitative phase-field crystal modeling of solid-liquid structures. *JOM*, 67:186–201, 2015.

[8] E. Asadi and M. Asle Zaeem. Quantitative phase-field crystal modeling of solid-liquid interfaces for FCC metals. *Comput. Mater. Sci.*, 127:236–243, 2017.

[9] M. Asta, J.J. Hoyt, and A. Karma. Calculation of alloy solid-liquid interfacial free energies from atomic-scale simulations. *Phys. Rev. B*, 66:100101, 2002.

[10] G.H. Bishop and B. Chalmers. A Coincidence–Ledge–Dislocation description of grain boundaries. *Scr. Metall.*, 2(2):133–139, 1968.

[11] F.P. Buff, R.A. Lovett, and F.H. Stillinger Jr. Interfacial density profile for fluids in the critical region. *Phys. Rev. Lett.*, 15(15):621–623, 1965.

[12] V.V. Bulatov, B.W. Reed, and M. Kumar. Grain boundary energy function for fcc metals. *Acta Mater.*, 65:161–175, 2014.

[13] J.W. Cahn and J.E. Hilliard. Free energy of a nonuniform system. I. Interfacial free energy. *J. Comput. Phys.*, 28:258–267, 1958.

[14] P.Y. Chan, N. Goldenfeld, and J. Dantzig. Molecular dynamics on diffusive time scales from the phase-field-crystal equation. *Phys. Rev. E*, 79:035701, 2009.

[15] S. Chandra, M.K. Samal, and V.M Chavan. Dislocation nucleation from damaged grain boundaries in face centered cubic metals – An atomistic study. *Materialia*, 8:100497, 2019.

[16] L.Q. Chen and J. Shen. Applications of semi-implicit Fourier-spectral method to phase field equations. *Computer Physics Communications*, 108:147–158, 1998.

[17] K.R. Elder and M. Grant. Modeling elastic and plastic deformations in nonequilibrium processing using phase field crystals. *Phys. Rev. E*, 70:051605, 2004.

[18] K.R. Elder, M. Katakowski, M. Haataja, and M. Grant. Modeling elasticity in crystal growth. *Phys. Rev. Lett.*, 88(24):245701, 2002.

[19] K.R. Elder, N. Provatas, J. Berry, P. Stefanovic, and M. Grant. Phase-field crystal modeling and classical density functional theory of freezing. *Phys. Rev. B*, 75:064107, 2007.

[20] H. Emmerich, H. Löwen, R. Wittkowski, T. Gruhn, G.I. Tóth, G. Tegze, and L. Gránásy. Phase-field-crystal models for condensed matter dynamics on atomic length and diffusive time scales: an overview. *Adv. Phys.*, 61(6):665–743, 2012.

[21] M.P.A. Fisher, D.S. Fisher, and J.D. Weeks. Agreement of capillary-wave theory with exact results for the interface profile of the two-dimensional Ising model. *Phys. Rev. Lett.*, 48(5):368, 1982.

[22] S.M. Foiles and J.J. Hoyt. Computation of grain boundary stiffness and mobility from boundary fluctuations. *Acta Mater.*, 54:3351–3357, 2006.

[23] N. A. Gjostein and F. N. Rhines. Absolute interfacial energies of [001] tilt and twist grain boundaries in copper. *Acta Metall.*, 7:319–330, May 1959.

[24] M. Greenwood, N. Provatas, and J. Rottler. Free energy functionals for efficient phase field crystal modeling of structural phase transformations. *Phys. Rev. Lett.*, 105:045702, 2010.

[25] M. Greenwood, C. Sinclair, and M. Militzer. Phase field crystal model of solute drag. *Acta Mater.*, 60:5752–5761, 2012.

[26] H. Hallberg. Approaches to modeling of recrystallization. *Metals*, 1:16–48, 2011.

[27] H. Hallberg and V.V. Bulatov. Modeling of grain growth under fully anisotropic grain boundary energy. *Modell. Simul. Mater. Sci. Eng.*, 27(4):045002, 2019.

[28] C. Herring. *The physics of powder metallurgy*, chapter 8, pages 143–179. McGraw-Hill, 1951.

[29] J.J. Hoyt, M. Asta, and A. Karma. Atomistic and continuum modeling of dendritic solidification. *Mater. Sci. Eng. R*, 41:121–163, 2003.

[30] Z.-F. Huang, K.R. Elder, and N. Provatas. Phase-field-crystal dynamics for binary systems: Derivation from dynamical density functional theory, amplitude equation formalism, and applications to alloy heterostructures. *Phys. Rev. E*, 82:021605, 2010.

[31] A. Jaatinen, C.V. Achim, K.R. Elder, and T. Ala-Nissila. Phase field crystal study of symmetric tilt grain boundaries of iron. *Technische Mechanik*, 30(1-3):169–176, 2010.

[32] O. Kapikranian, H. Zapolsky, C. Domain, R. Patte, C. Pareige, B. Radiguet, and P. Pareige. Atomic structure of grain boundaries in iron modeled using the atomic density function. *Phys. Rev. B*, 89:014111, 2014.

[33] C.L. Kelchner, S.J. Plimpton, and J.C. Hamilton. Dislocation nucleation and defect structure during surface indentation. *Phys. Rev. B*, 58(17):11085–11088, 1998.

[34] H.-K. Kim, S.G. Kim, W. Dong, I. Steinbach, and B.-J. Lee. Phase-field modeling for 3D grain growth based on a grain boundary energy database. *Modell. Simul. Mater. Sci. Eng.*, 22:034004, 2014.

[35] H.-K. Kim, W.-S. Ko, H.-J. Lee, S.G. Kim, and B.-J. Lee. An identification scheme of grain boundaries and construction of a grain boundary energy database. *Scr. Mater.*, 64(12):1152–1155, 2011.

[36] A.E. Lobkovsky, A. Karma, M.I. Mendelev, M. Haataja, and D.J. Srolovitz. Grain shape, grain boundary mobility and the Herring relation. *Acta Mater.*, 52:285–292, 2004.

[37] J. Mellenthin, A. Karma, and M. Plapp. Phase-field crystal study of grain-boundary premelting. *Phys. Rev. B*, 78:184110, 2008.

[38] H. Miura, M. Kato, and T. Mori. Temperature dependence of the energy of Cu [110] symmetrical tilt grain boundaries. *J. Mater. Lett.*, 13:46–48, 1994.

[39] S.K. Mkhonta, K.R. Elder, and Z.-F. Huang. Exploring the complexworld of two-dimensional ordering with three modes. *Phys. Rev. Lett.*, 111:035501, 2013.

[40] R.D. Moore, T. Beecroft, G.S. Rohrer, C.M. Barr, E.R. Homer, K. Hattar, B.L. Boyce, and F. Abdeljawad. The grain boundary stiffness and its impact on equilibrium shapes and boundary migration: Analysis of the σ5, 7, 9, and 11 boundaries in Ni. *Acta Mater.*, 218:117220, 2021.

[41] A. Movahedi-Rad and R. Alizadeh. Simulating grain boundary energy using molecular dynamics. *Journal of Modern Physics*, 5:627–632, 2014.

[42] D.L. Olmsted, S.M. Foiles, and E.A. Holm. Survey of computed grain boundary properties in face-centered cubic metals: I. Grain boundary energy. *Acta Mater.*, 57:3694–3703, 2009.

[43] J.L. Priedeman, C.W. Rosenbrock, O.K. Johnson, and E.R. Homer. Quantifying and connecting atomic and crystallographic grain boundary structure using local environment representation and dimensionality reduction techniques. *Acta Mater.*, 161:431–443, 2018.

[44] T.V. Ramakrishnan and M. Yussouff. First-principles order-parameter theory of freezing. *Phys. Rev. B*, 19(5):2775–2794, 1979.

[45] J.D. Rittner and D.N. Seidman. ⟨110⟩ symmetric tilt grain-boundary structures in fcc metals with low stacking-fault energies. *Phys. Rev. B*, 54(10):6999–7015, 1996.

[46] G.S. Rohrer. Grain boundary energy anisotropy: a review. *J. Mater. Sci.*, 46:5881–5895, 2011.

[47] L.S. Shvindlerman and B.B. Straumal. Regions of existence of special and non-special grain boundaries. *Acta Metall.*, 33(9):1735–1749, 1985.

[48] H.M. Singer and I. Singer. Analysis and visualization of multiply oriented lattice structures by a two-dimensional continuous wavelet transform. *Phys. Rev. E*, 74:031103, 2006.

[49] A.P. Sutton and V. Vitek. On the structure of tilt grain boundaries in cubic metals I. Symmetrical tilt boundaries. *Phil. Trans. R. Soc., London A*, 309(1506):1–36, 1983.

[50] Z.T. Trautt and M. Upmanyu. Direct two-dimensional calculations of grain boundary stiffness. *Scr. Mater.*, 52:1175–1179, 2005.

[51] M.A. Tschopp, S.P. Coleman, and D.L. McDowell. Symmetric and asymmetric tilt grain boundary structure and energy in Cu and Al (and transferability to other fcc metals). *Integr. Mater. Manuf. Innov.*, 4(11):1–14, 2015.

[52] M.A. Tschopp and D.L. McDowell. Asymmetric tilt grain boundary structure and energy in copper and aluminium. *Phil. Mag.*, 87(25):3871–3892, 2007.

[53] M.A. Tschopp, D.E. Spearot, and D.L. McDowell. *Dislocations in Solids*, volume 14, chapter 82, pages 46–139. North-Holland, 2008.

[54] M. Upmanyu. Grain boundary stiffness based on a dislocation model. *Scr. Mater.*, 56:553–556, 2007.

[55] S. van Teeffelen, R. Backofen, A. Voigt, and H. Löwen. Derivation of the phase-field-crystal model for colloidal solidification. *Phys. Rev. E*, 79:051404, 2009.

[56] N. Wang, Y. Ji, Y. Wang, Y. Wen, and L.-Q. Chen. Two modes of grain boundary pinning by coherent precipitates. *Acta Mater.*, 135:226–232, 2017.

[57] A.V. Weckman and B.F. Demyanov. Basic structural units of tilt grain boundaries. II. Misorientation axes [110] and [111]. *Physics of the Solid State*, 63(1):54–63, 2019.

[58] J.D. Weeks. Structure and thermodynamics of the liquid-vapor interface. *J. Chem. Phys.*, 67(1):3106–3121, 1977.

[59] D. Wolf. Structure-energy correlation for grain boundaries in F.C.C metals—III. symmetrical tilt boundaries. *Acta Metall. Mater.*, 38(5):781–790, 1990.

[60] K.-A. Wu, A. Adland, and A. Karma. Phase-field-crystal model for fcc ordering. *Phys. Rev. E*, 81:061601, 2010.

[61] A. Yamanaka, K. McReynolds, and P.W. Voorhees. Phase field crystal simulation of grain boundary motion, grain rotation and dislocation reactions in a BCC bicrystal. *Acta Mater.*, 133:160–171, 2017.

[62] S. Yoon, D. Jeong, C. Lee, H. Kim, S. Kim, H.G. Lee, and J. Kim. Fourier-spectral method for the phase-field equations. *Mathematics*, 8:1385, 2020.

[63] H. Zhang, D. Du, and D.J. Srolovitz. Determination of grain boundary stiffness from molecular dynamics simulation. *Appl. Phys. Lett.*, 88:121927, 2006.

[64] L. Zhang, C. Lu, K. Tieu, L. Pei, X. Zhao, and Kuiyu Cheng. Molecular dynamics study on the grain

boundary dislocation source in nanocrystalline copper under tensile loading. *Mater. Res. Express*, 2:035009, 2015.